

RESEARCH ARTICLE SUMMARY

BACTERIOPHAGE

Removal of *Pseudomonas* type IV pili by a small RNA virus

Jirapat Thongchol[†], Zihao Yu[†], Laith Harb, Yiruo Lin, Matthias Koch, Matthew Theodore, Utkarsh Narsaria, Joshua Shaevitz, Zemer Gitai, Yinghao Wu, Junjie Zhang*, Lanying Zeng*

INTRODUCTION: Retractable pili in bacteria play an important role in numerous biological processes, such as DNA and protein transfer, motility, adhesion, surface sensing, biofilm formation, and pathogenesis. Single-stranded RNA (ssRNA) bacteriophages (phages) are small viruses that specifically target these retractile pili. With a small positive-strand RNA genome of approximately 4000 nucleotides, ssRNA phages typically encode four proteins: maturation protein (Mat), coat protein (Coat), RNA-dependent RNA replicase (Rep), and single-gene lysis protein (Sgl). The Mat is crucial for phage maturity and pilus recognition. However, how ssRNA phages use the Mat-pilus interaction to enter the host cell has remained mysterious for the more than six decades since the discovery of the first ssRNA phage.

RATIONALE: The ssRNA phage PP7 infects *Pseudomonas aeruginosa* O1 (PAO1) through the type IV pilus (T4P), a prominent virulence factor associated with motility. Unveiling the mechanisms under which PP7 exploits T4P for cellular entry will shed light on fundamental aspects of phage-bacterium interactions and

phage biology and may open an avenue for antimicrobial strategies.

RESULTS: Using fluorescence microscopy, we observed the detachment of PAO1 T4P during PP7 infection. Intriguingly, T4P detachment induced by ultraviolet (UV)-inactivated PP7 (UV-PP7), whose viral RNA cannot enter the cell, mirrors that of the wild-type (WT) PP7. This indicates that T4P detachment occurs at the cell envelope during PP7 entry, independently of PP7 replication inside the cell. Alongside T4P detachment, both WT PP7 and UV-PP7 treatments impede T4P dynamics. This combined effect drastically reduces cell twitching motility.

PP7 mature virions, resolved by means of single-particle cryo-electron microscopy, feature two Mat proteins forming a heterotypic dimer. One Mat is exposed for T4P interaction, whereas the other is entirely internalized within the capsid. This mature PP7 virion structure diverges substantially from the single-Mat structure found in canonical *Escherichia coli* phages, such as MS2 and Q β , challenging our understanding of the structure of mature ssRNA phages.

To delve into the phage entry mechanism, we determined the structures of T4P and the PP7/T4P complex, which revealed that PP7 binds to T4P by interacting with a single pilin subunit through the Pilus-Interacting Region (PIR) of the Mat.

Through examination of various mutants of the host retraction ATPases and the pilus, we discovered that pilus detachment is influenced by the pilus retraction force and speed, as well as the affinity between phage Mat and its bound pilin. Further mechanical considerations led to the pilus bending hypothesis, which was substantiated by our Langevin dynamics simulation of the Mat bound to T4P during the phage entry process.

CONCLUSION: We observed that T4P can be detached or removed by an ssRNA phage and revealed the molecular mechanism for T4P detachment. We propose that similar mechanisms are widespread among ssRNA phages and their respective retractile pilus systems. Recent bioinformatic studies of environmental samples have identified thousands of ssRNA phage genomes, which await mechanistic analysis. This work could serve as a benchmark for investigating other phage and virus systems of different organisms. ■

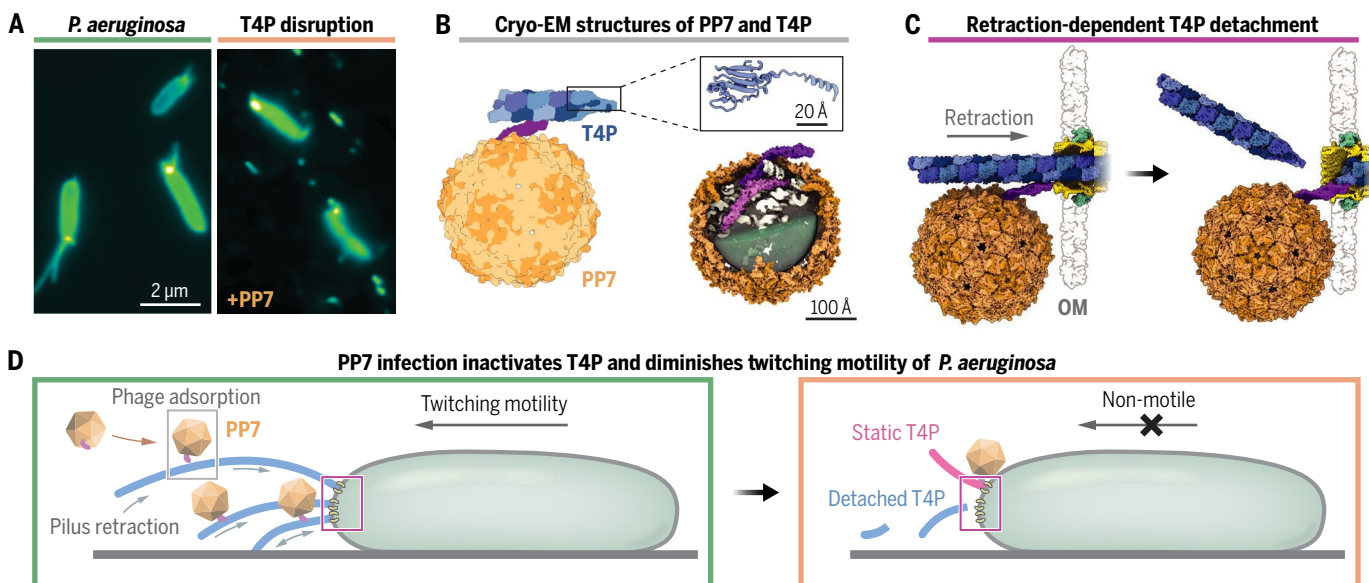
The list of author affiliations is available in the full article online.

*Corresponding author. Email: junjie@tamu.edu (J.Z.); lzeng@tamu.edu (L.Z.)

[†]These authors contributed equally to this work.

Cite this article as J. Thongchol *et al.*, *Science* **384**, eadl0635 (2024). DOI: 10.1126/science.adl0635

S READ THE FULL ARTICLE AT
<https://doi.org/10.1126/science.adl0635>



PP7 infection impairs *P. aeruginosa* motility. (A) Fluorescence images showing that T4P are detached upon PP7 infection. (B) Structures of PP7, T4P, and the PP7/T4P complex are resolved with single-particle cryo-electron microscopy. (C) PP7 hijacks T4P retraction for infection and detaches T4P. (D) Cell twitching motility is impaired owing to pilus detachment and nonfunctional T4P (the schematic diagram is not drawn to scale).

RESEARCH ARTICLE

BACTERIOPHAGE

Removal of *Pseudomonas* type IV pili by a small RNA virus

Jirapat Thongchol^{1,2†}, Zihao Yu^{1,2†}, Laith Harb^{1,2}, Yiruo Lin³, Matthias Koch^{4,5,6,7}, Matthew Theodore^{1,2}, Utkarsh Narsaria^{1,2}, Joshua Shaevitz^{4,6}, Zemer Gitai⁵, Yinghao Wu⁸, Junjie Zhang^{1,2*}, Lanying Zeng^{1,2*}

The retractile type IV pilus (T4P) is important for virulence of the opportunistic human pathogen *Pseudomonas aeruginosa*. The single-stranded RNA (ssRNA) phage PP7 binds to T4P and is brought to the cell surface through pilus retraction. Using fluorescence microscopy, we discovered that PP7 detaches T4P, which impairs cell motility and restricts the pathogen's virulence. Using cryo-electron microscopy, mutagenesis, optical trapping, and Langevin dynamics simulation, we resolved the structure of PP7, T4P, and the PP7/T4P complex and showed that T4P detachment is driven by the affinity between the phage maturation protein and its bound pilin, plus the pilus retraction force and speed, and pilus bending. Pilus detachment may be widespread among other ssRNA phages and their retractile pilus systems and offers new prospects for antibacterial prophylaxis and therapeutics.

Pili are proteinaceous structures on the surface of many bacteria, which play a crucial role in several essential processes for bacterial virulence, such as DNA and protein transfer, motility, biofilm formation, surface sensing, and pathogenesis (1–4). Pili are categorized into different classes on the basis of their structure and function (4). For example, the conjugative F-pili of *Escherichia coli* form an 87-Å-wide hollow helical filament (5) and have a characteristic retraction speed of ~16 nm/s (6) or ~48 nm/s (7), whereas the type IV pili (T4P) of *Pseudomonas aeruginosa*, an opportunistic human pathogen, have a 60-Å-wide solid helical filament (8) and a much faster retraction speed of ~650 nm/s (9).

Single-stranded RNA (ssRNA) phages, belonging to the family Fiersviridae, use retractile pili to infect bacteria. They carry a single copy of positive-strand viral RNA (vRNA) of approximately 4000 nucleotides (10). Typically, they encode four proteins: maturation protein (Mat), coat protein (Coat), RNA-dependent RNA replicase (Rep), and single-gene lysis

protein (Sgl) (11). Despite being known for approximately six decades, the structures of mature virions have been reported for only two ssRNA phages: the F-specific coliphage MS2 (Emesvirus) and Q β (Qubevirus) (12–16). They assemble into near-icosahedral with triangulation (T) number of three (T=3) particles measuring ~25 nm in diameter and consist of 178 (MS2) or 180 (Q β) copies of Coat, with a single copy of Mat. The ssRNA phage infection starts with the binding of phage Mat protein to the side of a pilus (14). In the case of F-specific coliphages MS2 and Q β , the infection process was shown to be associated with F-pilus detachment (17). Pilus retraction brings the pilus-bound phage to the cell surface, facilitating the delivery of vRNA from the phage capsid to the cell through an unknown mechanism (18).

PP7 detaches *P. aeruginosa* T4P during phage entry

To detect and quantify T4P in the PP7 host *P. aeruginosa* strain O1 (PAO1), we used a previously established strain (ZG1587) with a single cysteine substitution (A86C, in which alanine at position 86 was replaced with cysteine) in the *pilA* gene, encoding the major pilin subunit of the T4P filament, which enables labeling with thiol-specific fluorescent dyes (9) (fig. S1A). We observed an increase of free T4P present in the media with PP7 infection compared with buffer alone (Fig. 1A). This detachment is rapid and, for a multiplicity of infection (MOI) of 5, mostly occurs within 10 min after infection, reaching a plateau at ~3.9 pili per cell at 20 min after infection (Fig. 1B and fig. S1B), indicating that the early stage of PP7 infection leads to the release of T4P. Cysteine modification and dye labeling

do not affect PP7 infection, as evidenced by the similar plaquing efficiency to the wild-type (WT) parental strain (ZG1583) (fig. S1C).

To determine the critical step(s) for pilus detachment during PP7 infection, we dissected the PP7 infection into four steps: (i) phage adsorption to the pilus, (ii) phage vRNA pre-entry near the cell surface, (iii) phage vRNA translocation through the cell envelope into the cytoplasm, and (iv) phage replication inside the cell (Fig. 1C). For this purpose, we used both WT PP7 and ultraviolet-treated PP7 (UV-PP7). The latter completely lost its infectivity owing to cross-linking of the vRNA with the phage capsid (fig. S1, C and D). Therefore, UV-PP7 allows differentiation between phage adsorption and vRNA preentry steps from the steps of vRNA entry into cell cytoplasm and replication.

To visualize PP7 vRNA dynamics, we quantified PP7 RNA using single-molecule fluorescence in situ hybridization (smFISH) with probes targeting the full PP7 genome. We used a low MOI of ~0.5 to ensure that the great majority of infected cells were exposed to only one phage according to Poisson distribution (fig. S1E). Upon PP7 infection, single fluorescent foci corresponding to cell-associated PP7 RNA were observed at 1 and 5 min after infection (Fig. 1D). These foci likely represent the phage-encapsidated vRNA at the cell surface or the vRNA that has entered the cell. These foci were predominantly localized at the cell poles, where pili are present (Fig. 1E). At 10 and 20 min, an increased number of foci and larger clusters of fluorescent signals appeared compared with those at 5 min, presumably representing replicated RNA. These signals were found at both the cell poles and nonpolar regions, supporting the notion of intracellular diffusion and replication of the PP7 vRNA (Fig. 1, D and E, and fig. S2A). By contrast, the UV-PP7 vRNAs were predominantly localized at the cell pole, consistently accounting for ~85.7% of the observed population over time (Fig. 1, D and E). The remaining percentage can be attributed to the presence of nonpolar pili (fig. S1F). Furthermore, the fluorescence intensity of individual spots remained constant over time, which is indicative of a single RNA molecule (fig. S1G). It appears that UV-PP7 vRNA is unable to move within the cell or to replicate. During the smFISH assay, vigorous centrifugation and wash steps were used that likely removed the extracellular portion of the pilus. This observation indicates that the RNAs we observed at the cell pole (Fig. 1D) were likely due to the UV-PP7 particles trapped near the outer membrane at the channel of the pilus assembly machine (Fig. 1C).

At an MOI of 0.5, the percentage of cells positive for UV-PP7 (cells containing fluorescent foci) is the same as that of the WT PP7,

¹Department of Biochemistry and Biophysics, Texas A&M University, College Station, TX 77843, USA. ²Center for Phage Technology, Texas A&M University, College Station, TX 77843, USA. ³Department of Computer Science and Engineering, Texas A&M University, College Station, TX 77843, USA. ⁴Lewis-Sigler Institute for Integrative Genomics, Princeton University, Princeton, NJ 08544, USA. ⁵Department of Molecular Biology, Princeton University, Princeton, NJ 08544, USA. ⁶Joseph Henry Laboratories of Physics, Princeton University, Princeton, NJ 08544, USA. ⁷Department of Biology, Texas A&M University, College Station, TX 77843, USA. ⁸Department of Systems and Computational Biology, Albert Einstein College of Medicine, NY 10461, USA.

*Corresponding author. Email: junjiez@tamu.edu (J.Z.); lzeng@tamu.edu (L.Z.)

†These authors contributed equally to this work.

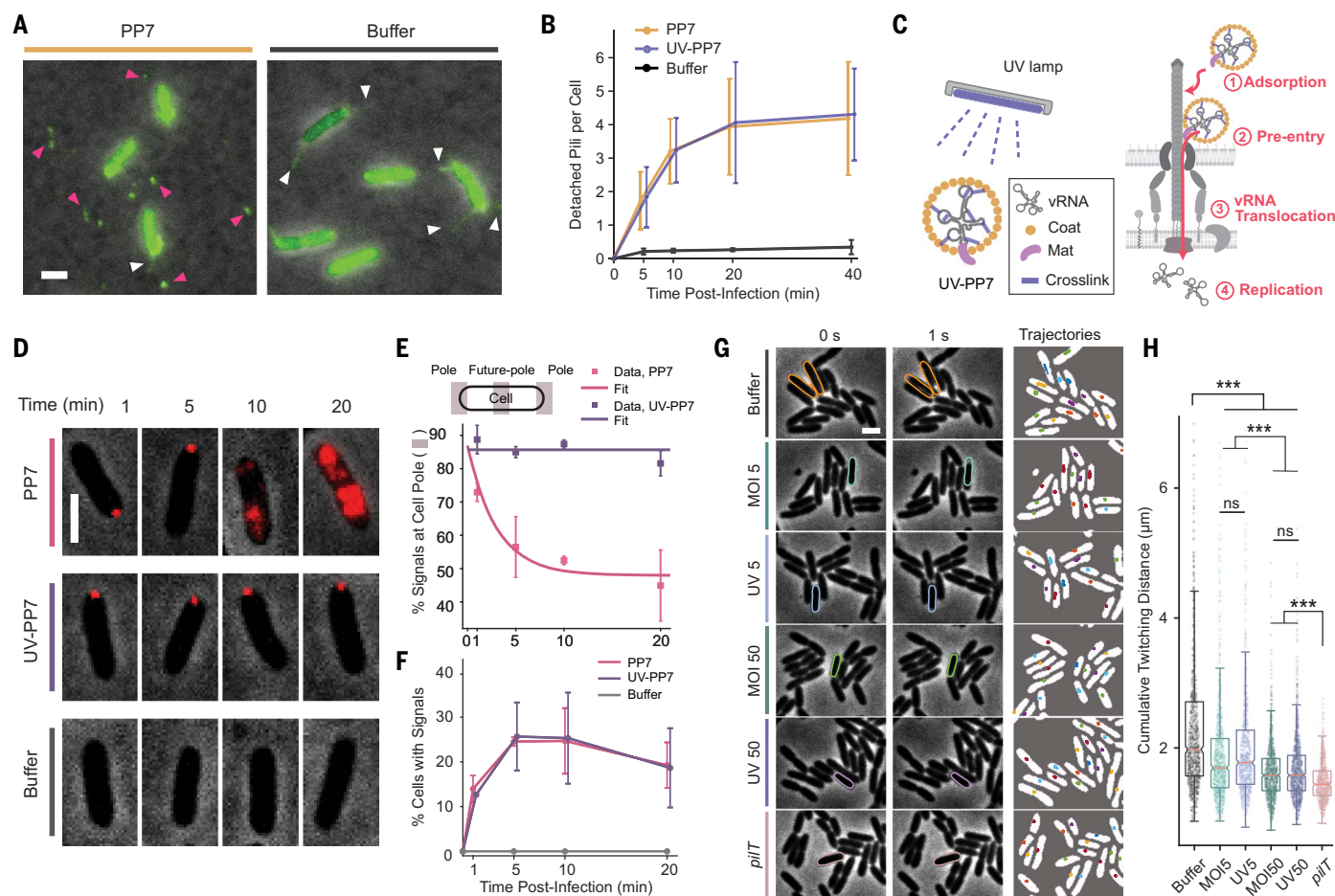


Fig. 1. PP7 detaches *P. aeruginosa* T4P and immobilizes *P. aeruginosa* cells.

(A) Representative images of detached T4P (some indicated with red arrowheads) resulting from PP7 infection compared with buffer treatment with cell-associated pili (indicated with white arrowheads). (B) Detached pili increase over time before plateauing at ~3.9 pili per cell after cells are infected by PP7 at MOI = 5 or equivalent UV-PP7. Total number of pili per cells at 5, 10, 20, and 40 min were for PP7, 3222/1850, 4185/1315, 5075/1403, and 1187/4661, respectively; UV-PP7, 1512/1109, 3820/1151, 3209/1163, and 3654/958, respectively; and buffer, 227/1202, 249/1054, 236/886, and 303/881. PP7 and UV-PP7 treatment experiments were performed with at least six biological replicates. Buffer control was repeated with three replicates. (C) Schematic of PP7 with UV treatment and PP7 infection process. (D) Representative images of PP7 RNA (red) detected by smFISH at MOI = 0.5. (Top) The RNA of PP7 infected cells replicates over time, whereas (middle) that of UV-PP7 infected cells remains as a single focus compared with (bottom) no RNA in the uninfected control. (E) The percentage of cells with polar RNA of the total cells with RNA signals. The RNA signal with UV-PP7 infection stays at ~85% over time, whereas that with PP7 infection follows an exponential decay, $y = 47.96 + 38.98\exp(-0.334x)$. (F) The percentage

of cells with RNA signals upon PP7 infection is similar to that of UV-PP7. Total number of cells at 1, 5, 10, and 20 min were for PP7, 2372, 6475, 2285, and 3251, respectively; UV-PP7, 2005, 7421, 2380, and 3952, respectively; and buffer, 690, 3490, 3048, and 2172, respectively. RNA FISH data in (E) and (F) represents the same set of experiments that composite at least two biological replicates for each time point. (G) (Left, middle) Representative phase-contrast snapshots illustrating cell twitching activities with buffer and phage infection for 5 min. The colored cell contours represent those at 0 s. (Right) Colored lines depicting the trajectory of each cell's centroid for the 1-min movie with 1 s imaging interval. Scale bar, 5 μ m. (H) Box plots showing the distribution of cell centroid movement overlaid with swarm plots for data for individual cells from two biological replicates. Number of tracked cells were for buffer 998; MOI 5, 903; UV 5, 846; MOI 50, 978; UV 50, 1081; *pilT*, 648. PP7 and UV-PP7 infection cause the same reduction of cell motility. Asterisks denote statistical significance by use of Student's *t* test ($***P < 0.001$; ns, not significant). The Tukey-style box plot shows interquartile range (IQR) divided by the median (red line), and the whiskers extend to $1.5 \times$ IQR. Scale bars, 2 μ m. All error bars in this figure indicate SD. Data points are slightly offset to avoid overlap as necessary.

indicating that UV treatment does not affect the adsorption of PP7 particles to the T4P. The adsorption is concluded within 5 min of infection, indicated by the plateaued percentage of cells with RNA signals at ~23.0% (Fig. 1F and fig. S1H). The slight decrease at 20 min is likely due to the growth of cells, especially the uninfected cells, over this time (fig. S1I). Furthermore, WT PP7 vRNA has already started

to enter and diffuse inside the cell at 1 min, resulting in a lower percentage of polar RNA relative to the nonmoving UV-PP7 vRNA (Fig. 1E). Additionally, more vRNAs entered the cell over time, with an exponential decay of cells containing fluorescent signals at the cell pole (Fig. 1E). A large portion (~44.9%) of cell-associated RNA signals with WT PP7 infection were still located at the cell pole at 20 min (Fig.

1E and figs. S1J and S2A), indicating a non-synchronous infection by PP7.

With UV-PP7 at an MOI of 5 (UV 5), the kinetics of pilus detachment was indistinguishable from that observed with WT PP7 (Fig. 1B and fig. S1K). The same is also true at MOIs of 0.5 and 10 (fig. S1L). The RNA smFISH results (Fig. 1, D and F) further corroborate the inability of UV-PP7 to deliver its vRNA into

the cell owing to the cross-linking of vRNA to the phage capsid (fig. S1D). Taking these results together, we concluded that pilus detachment occurs between the phage vRNA attachment near the cell surface and phage vRNA entry into the cell cytoplasm (Fig. 1C). Moreover, pilus detachment is independent of phage RNA replication inside the cell.

PP7 infection reduces cell motility

In *P. aeruginosa*, T4P mediates twitching motility through extension, tethering, and retraction to drive cell movement (1). Both extrinsic and intrinsic factors, such as media composition (19), production of biosurfactants (20), and number of pili (21) affect twitching motility. In light of the pilus detachment by PP7, we set out to explore how PP7 infection affects twitching motility.

At the single-cell level, healthy uninfected cells (ZG1587) undergoing twitching motility typically displayed bursts of linear movement, direction reversals, and snapping to parallel alignment with neighboring cells (movie S1), which is in agreement with the literature (22). However, at 5 min after infection, when phage vRNA preentry-entry plateaus (Fig. 1F), cells displayed infrequent twitching, with most cells appearing immobile, especially at a high MOI of 50 (Fig. 1G and movie S1). We segmented and tracked cells, which were imaged at 1-s intervals and quantified the cumulative twitching distance of each cell across 1 min (Fig. 1, G and H). PP7-infected cells moved significantly shorter distances, with a median of 1.69 μm for an MOI of 5 and 1.58 μm for an MOI of 50, compared with 1.97 μm for buffer alone. The twitching motility of individual cells exhibits great heterogeneity, as observed in a wide range of twitching distances. At the high MOI of 50, cells showed very limited movement, and the twitching distance is close to that for a pilus retraction-deficient mutant *pilT* (ZG1589, 1.44 μm). The background-level movement of *pilT* is the same as that of the *pilA* mutant (in which the *pilA* gene was removed) without pilus (JTB8F5, 1.45 μm), likely because of microscope stage drift during time-lapse movie imaging (Fig. 1H and fig. S3A). For cells “infected” by UV-PP7, we observed a similar level of motility reduction with 1.77 μm for UV 5 and 1.58 μm for UV 50 (Fig. 1H). The similar twitching reduction caused by UV-PP7 particles indicates that the inhibition of twitching motility happens rapidly before vRNA cellular entry (Fig. 1C).

By measuring the dynamic activity of pili, we found that PP7 and UV-PP7 infection result in the same level of inhibition of T4P, manifested by T4P detachment, static T4P, and accumulated pilin subunits at the cell poles, which contributed to the reduction of motility (fig. S3, B to E, and movie S2). In addition, the metabolic burden caused by PP7

replication inside the cell further reduces dynamic pili, and at 20 min after infection at an MOI of 50, cells become completely immobile (fig. S3, F to H, and movies S1 and S2).

One PP7 virion possesses two maturation proteins

We used single-particle cryo-electron microscopy (cryo-EM) to determine the structure of the PP7 virion at 3.86-Å resolution (fig. S4A and table S3). The overall architecture of the mature PP7 virion reveals a near icosahedral $T = 3$ capsid consisting of 178 Coat molecules, as observed in ssRNA coliphages (Fig. 2A). Unexpectedly, each mature PP7 virion contains two Mat molecules instead of one. One of these Mat proteins, designated Mat_{EX} (exposed Mat), disrupts the perfect icosahedral symmetry of the capsid at the twofold axes. The other Mat, referred to as Mat_{IN} (internalized Mat), is completely internalized, alongside the vRNA (Fig. 2, B and C, and movie S3).

Approximately 60% of the analyzed PP7 particles exhibited a clearly defined vRNA density within the capsid, accompanied by the presence of two Mat proteins. By contrast, the remaining 40% of particles contain 180 copies of Coat proteins but lack Mat molecules or defined structures for RNA. This is not surprising given that ssRNA phages are known to naturally form noninfectious virus-like particles (VLPs), as shown from cryo-EM studies (23). For those 60% of particles with two Mat molecules and well-defined vRNA density, we designated the position of the Mat proteins as the “north pole.” The vRNA resolvability in the “southern hemisphere” was lower than in the “northern hemisphere” (Fig. 2C). In this work, we identified at least five distinct vRNA conformations through focused classification (fig. S4B). Previous studies in ssRNA coliphages have reported different vRNA conformations, albeit primarily limited to a small region (13, 24). Our PP7 structures show diverse viral vRNA conformations within the capsid.

A pair of Mat molecules binds to the 3' end of vRNA

The two Mat proteins potentially stabilize vRNA in the northern hemisphere, leading to the better resolvability of vRNA density in the northern hemisphere (Fig. 2B). The detailed examination of the cryo-EM structure of the PP7 Mat molecule reveals a tripartite structure, comprising an α -helical region consisting of four α -helices, a major β -sheet region consisting of six antiparallel β -strands, and an extended minor β -sheet region containing five antiparallel β -strands (Fig. 2D). The two Mat molecules form a heterotypic homodimer, with the two minor β -sheet regions positioned at a 45° angle when viewed from the top. The intersubunit interactions between the two Mat

proteins primarily occur between the α -helical region of Mat_{EX} and the major β -sheet region of Mat_{IN} (Fig. 2F). Specifically, the $\beta 7$ strand of Mat_{IN} fits intricately into a hydrophobic groove formed between $\alpha 1$ and $\alpha 2$ of Mat_{EX} (Fig. 2G).

The 3' end of the vRNA binds to the Mat protein in mature virions and is essential for initiating the vRNA replication once it enters the host cytoplasm (16, 25). The last 95 nucleotides of PP7 (residues 3494 to 3588) adopt a domain structure containing a four-way junction consisting of three RNA stem-loops (denoted as U1, V, and U2) from the 3' untranslated region, preceded by the stem-loop R1 containing the UAG stop codon of the *rep* gene (Fig. 2E). This RNA domain interacts with the Mat dimer. The Mat dimer acts as forceps, firmly grasping onto this RNA domain, which in turn acts as a claw, latching onto the Mat dimer. The U1 and V loops weave through the β regions of the Mat dimer, with U1 interacting with the inner surface of the major β -sheet from Mat_{EX}, and V interacts with the outer surface of the minor β -sheet from Mat_{IN}. Additionally, R1 interacts with the inner surface of the major β -sheet from Mat_{IN} (Fig. 2F). These RNA-Mat interactions presumably further stabilize the Mat dimer. Although the complete atomic model for vRNA is unavailable, from our cryo-EM map we discerned that vRNA interacts primarily with the inner surface of the Coat protein shell (fig. S4C), which is consistent with findings from other ssRNA phages (13, 16). These intimate interactions between vRNA and the capsid (Mat and Coat proteins) could serve as sites for cross-linking in UV-PP7 (26–28), impeding the vRNA from exiting the capsid for cell entry (Fig. 1C).

PP7 interacts with PAO1 T4P through the minor β -region of Mat_{EX}

PP7 cannot infect *P. aeruginosa* strain K (PAK), despite high structural and sequence similarities between T4P_{PAO1} and T4P_{PAK} (figs. S5, A to C, and S6) (8). To reveal the molecular specificity of PP7 for T4P_{PAO1}, we determined the cryo-EM structure of T4P_{PAO1} and the PP7/T4P_{PAO1} complex (Fig. 3, A and B; figs. S7 and S8; and table S3). The Mat_{EX} minor β -sheet region of PP7 interacts with a *pilA* subunit within the T4P_{PAO1} filament, orienting the tip of Mat_{EX} toward the host cell. We called this minor β -region the Pilus-Interacting Region (PIR) (Figs. 2D and 3C and movie S4). The PIR interacted with PilA^{PAO1} through the variable $\beta 1\beta 2$ loop (PilA _{$\beta 1\beta 2$}), primarily by electrostatic forces. PIR exhibited an overall positive charge, whereas PilA _{$\beta 1\beta 2$} displayed an overall negative charge (fig. S5D).

To validate our structural findings, we generated chimeric PilA mutants by replacing each variable loop in PilA^{PAO1} with those from PAK. The chimeras showed that the crucial residues

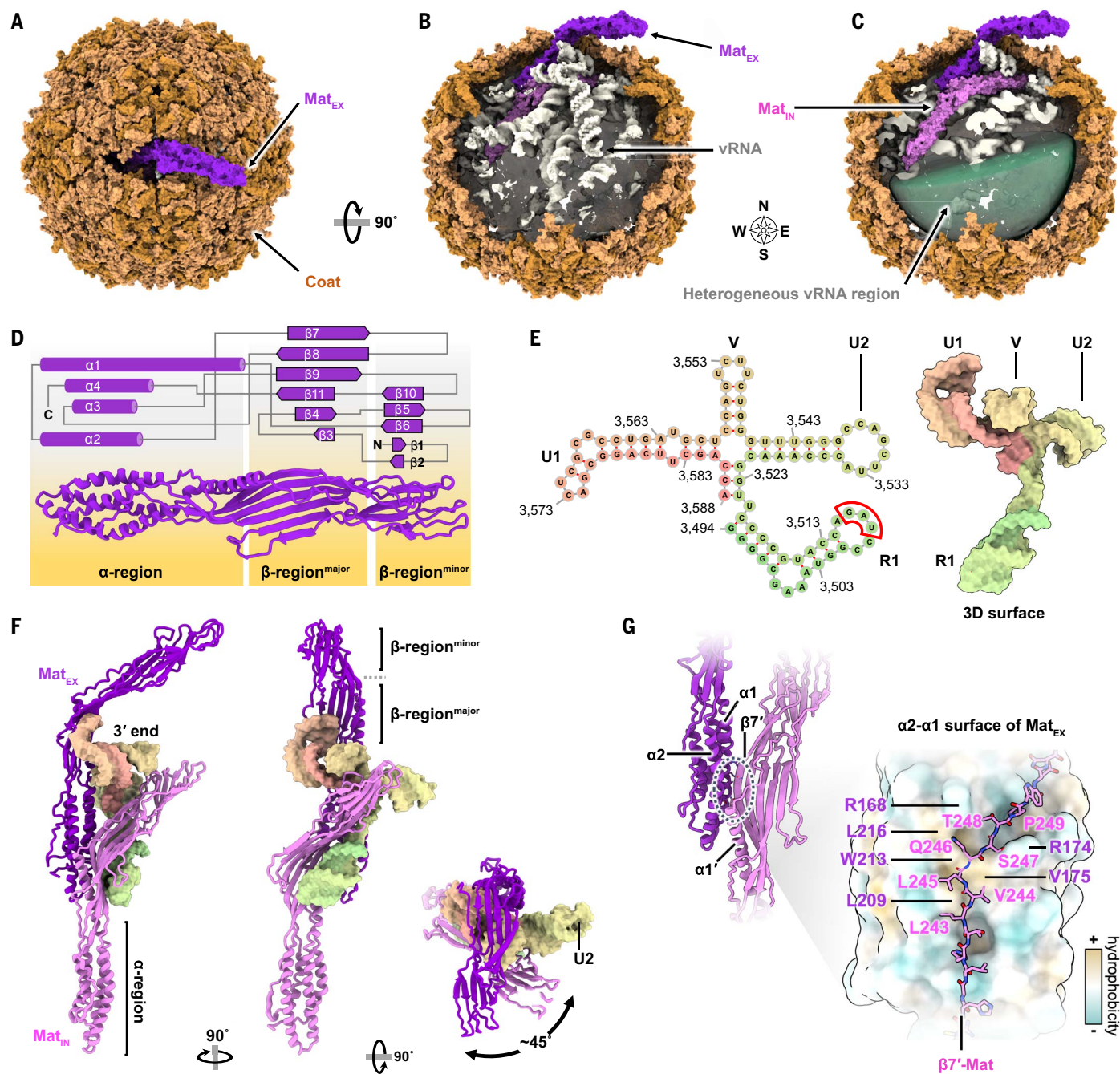


Fig. 2. The atomic model of PP7 mature virions that possess two Mat proteins. (A) The atomic model of PP7 mature virions shows a top view at the twofold axes, where Mat_{EX} (purple) breaks the perfect T=3 symmetry by replacing a coat dimer. The coat protein shell is colored orange. (B) The side view of the PP7 model, rotated 90° from (A), shows the mature virions with a partially removed capsid to reveal the cryo-EM density of vRNA (gray) and its two Mats: Mat_{IN} (pink) and Mat_{EX} (purple). The region of the particle where the Mat proteins are located is defined as the northern hemisphere. (C) The side view of the PP7 in the same orientation as in (B) with the vRNA partially removed to reveal the two Mats. The vRNA in the southern hemisphere (indicated with a transparent green semisphere) in the consensus map showed poor resolution owing to high heterogeneity. However, after further classification, we were able to resolve at least five

different conformations of this region, as further shown in fig. S4B. (D) The secondary structure topology of PP7 Mats that fold into three distinct regions, namely α -region, major β -region, and minor β -region. We chose Mat_{EX} as a representative. (E) The 3' end (nucleotide residues 3494 to 3588) of PP7 vRNA is shown as (left) a secondary structure and (right) 3D surface model. This 3' end folds into stem loops, namely U1, V, U2, and R1. The R1 loop contains the stop codon of the replicase gene (UAG, red box). (F) The cryo-EM structure of Mat proteins and 3' end. The interaction between Mat proteins and the 3' end involves the dimerization of two Mats and their interaction with the U, V1, and R1 loops of the 3' end of the vRNA. (G) The interactions between Mat proteins are mediated by the Mat_{EX} α -region that forms a small hydrophobic patch and the Mat_{IN} β 7-strand that fits into the patch.

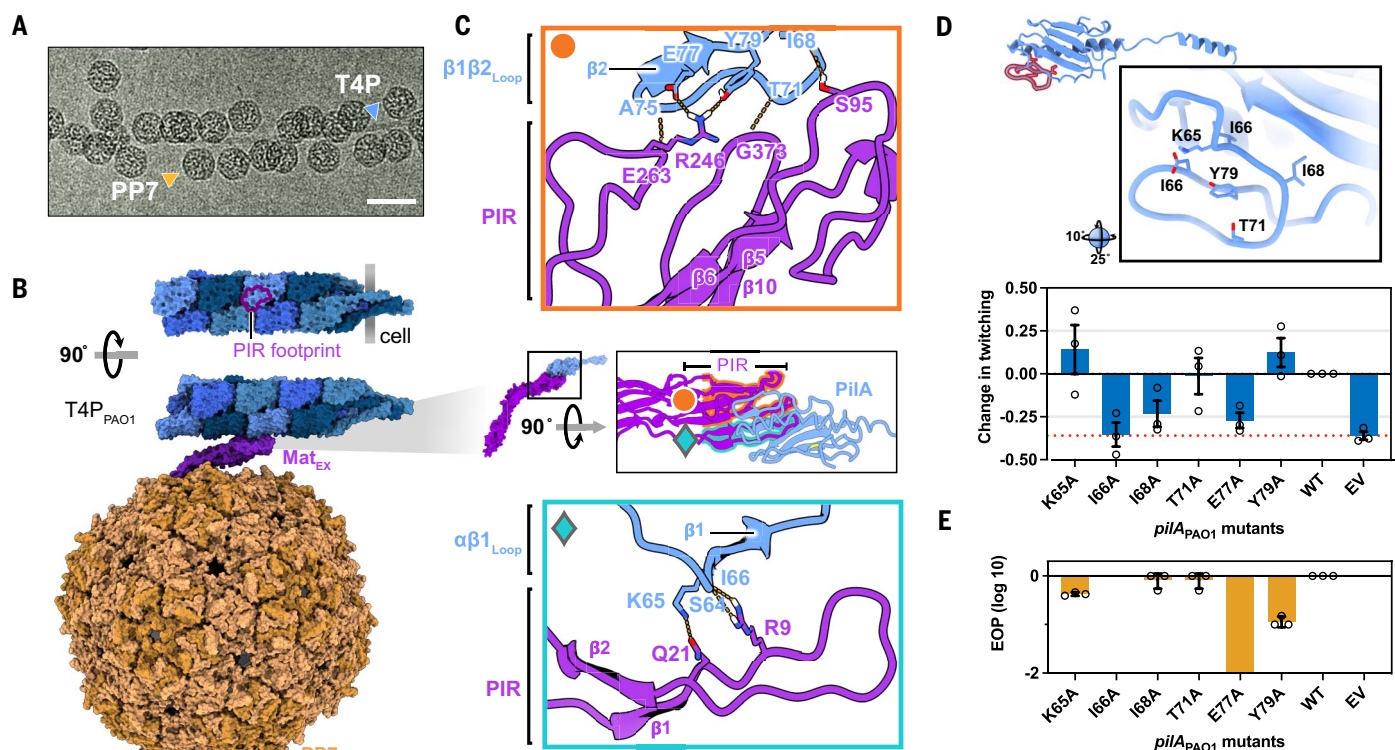


Fig. 3. PP7 specifically binds to T4P_{PAO1} interacting with one pilin subunit.

(A) A representative of electron micrographs of PP7 bound to purified T4P. Scale bar, 500 Å. (B) The atomic model of PP7/T4P complex showing PP7 uses its Mat_{EX} minor β-region to bind to a single pilin on T4P. The Mat_{EX} minor β-region is thus referred to as Pilus-Interacting Region (PIR). (C) The top view orientation of the interaction between PIR and a pilin (PilA) subunit. The interaction was mediated by specific interaction between PIR and the pilin region β1β2 loop (residues 65 to 79). The interactions were further zoomed in, as indicated with the circle and diamond. (D) (Top) The ribbon model of a

PilA subunit. (Inset) The red-highlighted region, where the amino acid residues for alanine-scanning mutagenesis were labeled. (Bottom) The twitching efficiency of *Pseudomonas* PAKΔ*pilA* strains from alanine scanning of those residues shown in (C) compared with WT *pilA*^{PAO1}. The red dotted line indicates the movement of PAKΔ*pilA* with empty vector (EV), which exhibits a basal level of movement as a negative control, such as cell expansion, but shows no movement in terms of twitching motility. (E) The EOP of PP7 from alanine scanning compared with WT *pilA*^{PAO1}; *n* = 3 biological replicates. The error bars indicate SD.

for binding are within the β1β2 loop (fig. S5, E and F). Using alanine substitution mutagenesis, we further identified K65 and Y79 as critical residues (K, lysine; Y, tyrosine) that determine PP7 specificity for PilA^{PAO1} (Fig. 3, D and E, and fig. S8, B and C), which is in agreement with our cryo-EM structure of the PP7/T4P_{PAO1} complex (Fig. 3C).

T4P retraction force and speed control T4P detachment

PP7 relies on host pilus retraction for infection (18) mediated by the major retraction adenosine triphosphatase (ATPase) PilT and auxiliary retraction ATPase PilU (Fig. 4A and figs. S1C, S5A, and S9, A and B). These ATPases likely exert force to disrupt pilin-pilin interactions and facilitate vRNA penetration into the cell. To identify the roles that PilT and PilU play in phage-host interactions, we examined a series of mutant ATPases.

It has been reported that both *pilT*-D160N (D, aspartate; N, asparagine) and *pilU* mutants in the PAK strain have defects in twitching

motility (29). We introduced these two mutations into the PAO1 strain and found that *pilT*-D160N (MK148) has no observable twitching, whereas the transposon-inactivated *pilU* allele (MK122) has only residual twitching capacity at the single-cell level and a slightly larger twitching diameter than that of *pilT*, the retraction-deficient negative control (fig. S9C and movie S5). We then used optical trapping (30, 31) to measure the forces of these mutant strains and compared them with the wild type (ZG1587). The wild type generated an average retraction stall force of 48.9 pN, which is consistent with the previously published value (32). *pilT*-D160N and *pilU* variants produced an average stall force of 33.5 and 40.9 pN, respectively, which were significantly lower than that of the wild type (Fig. 4B). We called these two mutants the “retraction-force mutants.” The retraction forces measured for all the strains have a wide range, indicating stochasticity in the force output of each pilus by the ATPases. Upon PP7 infection, *pilT*-D160N and *pilU* mu-

nants only showed background T4P detachment (fig. S9A), which indicated that T4P detachment depended on pilus retraction force, requiring both retraction ATPases PilT and PilU for successful infection.

We then tested *pilT*-H222A with a T4P retraction speed three times slower as compared with that of the wild type (9) and called it a “retraction-speed mutant.” PP7 formed plaques on *pilT*-H222A (H, histidine; A, alanine; ZG1824) with similar efficiency (fig. S1C), and *pilT*-H222A twitches similarly (fig. S9C) to the wild type. At the single-cell level, *pilT*-H222A exhibited observable twitching, and its T4P was detached by PP7, although less extensively than in the wild type (Fig. 4C, fig. S9D, and movie S5). The reduced retraction speed exhibited by *pilT*-H222A translates to diminished power output by the T4P retraction motor (9) and likely underlies reduced pilus detachment and attenuation of twitching at the single-cell level (Fig. 4C). A reduction in retraction speed of *pilT*-H222A T4P affects similar retraction-dependent functions, such as substrate stiffness sensing (in

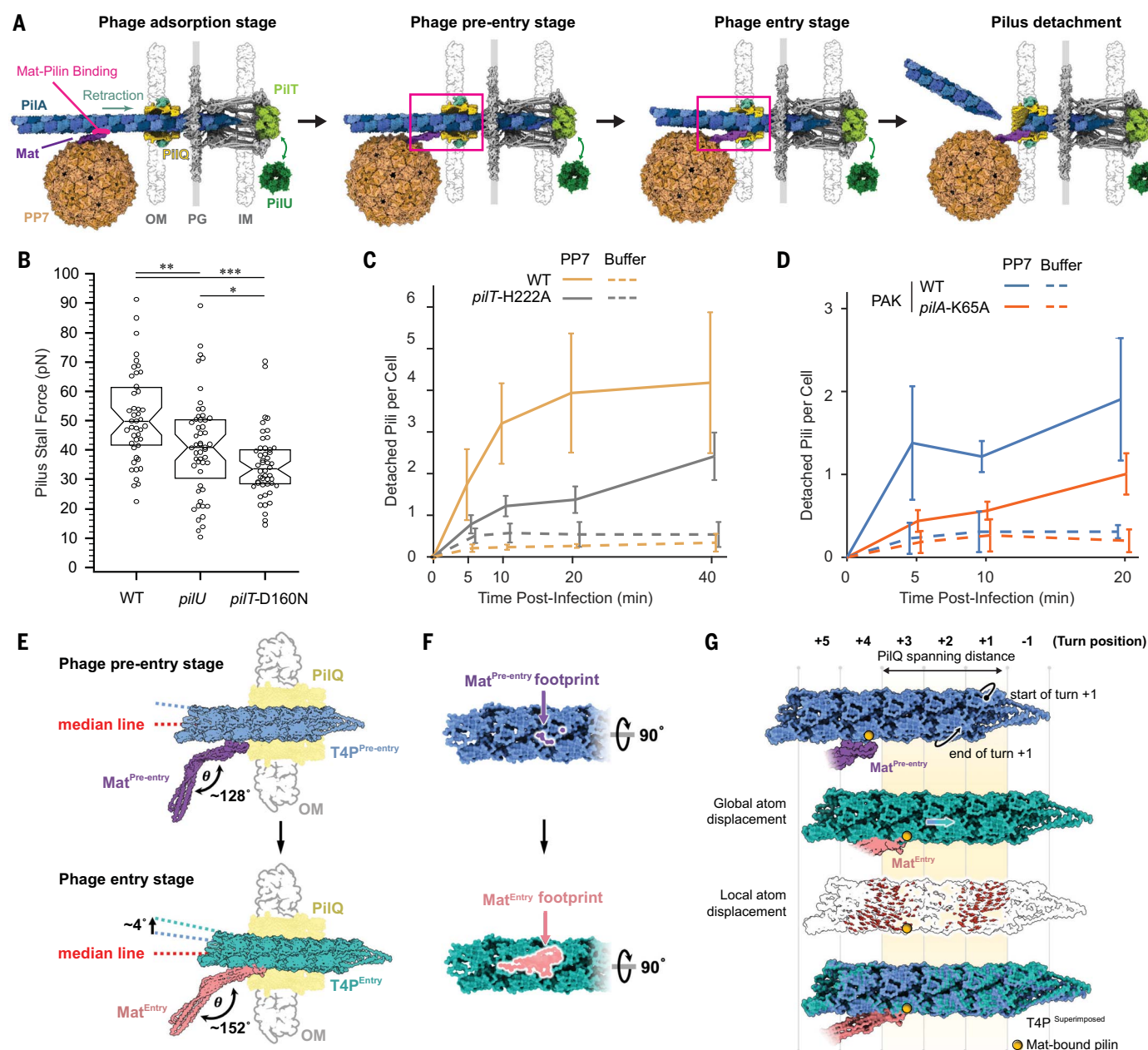


Fig. 4. Determinants and model for T4P detachment. (A) The schematic model depicting (left) the requirements for T4P detachment by PP7, including pilus retraction powered by ATPases PilT and PilU, and Mat-pilin interaction. After the adsorption on the pilus (left), (middle left) PP7 is brought to the cell surface by pilus retraction, and Mat enters the cell envelope, causing (middle right) pilus bending and (right) pilus detachment afterwards. The T4P machinery was created from the composite models by using PDB entries 3JC8, 6VE2, and 2EWV and AlphaFold-predicted PilU. OM, outer membrane; PG, peptidoglycan; IM, inner membrane. (B) Distribution of retraction stall forces of individual T4P with an average of 48.9 pN (WT, $n = 45$ individual T4P), 40.9 pN (*pilU*, $n = 51$ individual T4P), and 33.5 pN (*pilT-D160N*, $n = 48$ individual T4P). Asterisks indicate statistical significance by use of bootstrapped Mann-Whitney sample test; *** $P < 0.001$, ** $P < 0.01$, * $P < 0.05$. (C) PP7 can detach *pilT-H222A* pili although at a lower level than WT pili at MOI = 5. Total number of pili per cells for *pilT-H222A* at 5, 10, 20, and 40 min were for PP7, 519/700, 767/642, 782/583, and 1737/691, respectively, and buffer, 138/264, 156/278, 202/409, and 228/497,

respectively; Wild type from Fig. 1B is plotted for comparison. The experiments of PP7 infecting *pilT-H222A* and buffer were performed four times and twice, respectively. (D) The *pilA-K65A* mutation results in less detached pili than that in the WT. Total number of detached pili per cells at 5, 10, and 20 min were for wild type, 1575/1141, 1668/854, and 1821/1237, respectively; buffer, 140/737, 227/658, and 323/988, respectively; *pilA-K65A*, 509/1185, 628/1149, and 882/900, respectively; and buffer, 89/542, 162/644, and 186/858, respectively. Data represent two biological replicates. The error bars in (C) and (D) indicate SD. (E) The Langevin dynamics were used to simulate the T4P retraction events upon PP7 binding. The structures (top) before and (bottom) after the simulation were compared. The structure before the retraction event was configured as a phage preentry stage, in which PP7 Mat_{EX} (purple) binds to T4P (blue). Through the Langevin dynamics, the entry stage was revealed, in which the T4P (green) was pulled for one helical turn before further T4P retraction was blocked by Mat_{EX} (salmon). This blockage of Mat_{EX} in the PilQ causes a change in its conformational angle and results in the bending of T4P. (F) The contact

area between Mat_{EX} and T4P increased during the entry stage. The contact was determined by use of ChimeraX software, with a distance of ≤ 7 Å. **(G)** The analysis of T4P movement from the preentry to entry stages was performed with simulations. The original Mat-bound pilin is indicated with a yellow sphere. Global atom displacement indicates the average movement of C α atoms, excluding the outermost turns

(+5 and +1 turn of T4P) to avoid artifacts from the simulation. Local atom displacement illustrates the movement of individual C α atoms when aligning T4P between the preentry and entry stages, disregarding the +5 and +1 turns. The Movevectors plugin in PyMol was used to plot vectors with a distance cutoff of 1.5 Å, a vector sampling of 4, and a vector factor of 2.

which T4P retraction deforms the substrate) independently of force (32).

Mat-pilin interaction affects T4P detachment

We postulate that the Mat-pilin interaction must be strong enough to prevent the dissociation of phage particles before the force exerted on the pilin-pilin interaction reaches its breaking point (Fig. 4A, left). If true, a weaker Mat-pilin interaction would lead to less pilus detachment and consequently result in less productive PP7 infection. To test it, we examined the *pilA*-K65A mutant with a weaker Mat-pilin interaction (Fig. 3, D and E). The alanine substitution at the exposed K65 residue had no effect on pilin-pilin interaction because the twitching motility was unaffected (Fig. 3D). In addition, in the Δ PAK*pilA* background, the *pilA*-K65A mutant plasmid (JTB13A1) supported dynamic pilus production similar to that of its parental strain (JTB12A1) (movie S6), indicating that K65A does not influence pilin-pilin interaction. As expected, pilus detachment, cell-associated PP7 RNA, and the efficiency of plating (EOP) of *pilA*-K65A with PP7 infection were lower than those of its parental strain (Fig. 4D and figs. S1C and S9, E to G).

Langevin dynamics simulation captures priming pilus detachment

Our cryo-EM structures allow us to make a molecular model to test the impact of Mat binding to T4P_{PAO1} during retraction in silico. Leveraging the cryo-EM structure of *Pseudomonas* PilQ secretin (33), we computationally assembled a PilQ ring with the T4P passing through it. The PilQ channel exhibits an inner diameter of ~ 76 Å, accommodating a T4P of 60 Å wide. With a length of ~ 115 Å, the PilQ channel allows for three turns of pilins within it (Fig. 4E).

Upon infection, Mat_{EX} of PP7 binds to a pilin subunit on the extracellular side of PilQ and migrates along with the retracting T4P through the PilQ channel. Pilus detachment appears to occur at the outer-membrane complex where PilQ is located. This is supported by the inability of UV-PP7 to enter the cell but retaining the capacity to detach the T4P. The adsorption of PP7 to the pilus is predominantly driven by Mat_{EX}, whereas the detachment of the pilus occurs at the PilQ ring. These observations justify our simplified model that uses only the Mat-T4P-PilQ complex to investigate pilus detachment (Fig. 4A). We performed

a coarse-grained Langevin dynamics simulation for the C α atoms in the above system by describing the intramolecular interactions of the system as elastic networks to accommodate the flexibility and deformation of the channel and the Mat-T4P complex. After the retraction of T4P from the periplasmic side of the PilQ ring, we were able to capture the initial step of Mat entry into the PilQ ring alongside the T4P filament.

During this entry step (Fig. 4E), the PIR (minor β -sheet of Mat_{EX}) enters the PilQ channel along with the bound pilin. Simultaneously, the Mat undergoes substantial conformational change in the angle between the α -helical and β -sheet regions from 128° to 152°. The simultaneous entry of Mat and T4P into the narrow PilQ channel causes T4P to bend 4° away from the Mat-bound side, increasing the interaction area between Mat and T4P from 129 to 1315 Å² (Fig. 4F). In addition to the global movement of the T4P for approximately one helical rise toward the periplasm, each pilin locally deviates from their relative positions in the pilus, leading to the stretching and bending of the T4P at the Mat-bound site. This is intuitive because the Mat-T4P complex becomes stuck at the rim of the PilQ during the phage entry step because of its narrow inner diameter. Additionally, the retraction force continues to pull the pilins, causing their elongations and further destabilizing the pilin-pilin interaction (Fig. 4G), which leads to the final pilus detachment.

During the engagement of the relatively bulky pilus-bound phage with the distal end of the pilus channel, it may cause additional stress on the pilus as retraction continues. To accommodate the Mat-vRNA complex into the channel, T4P may become severed and released at the point of entry. After detachment, continued pilus retraction likely pulls the Mat-vRNA complex further through the cell envelope, followed by translocation of the vRNA into the host cytoplasm to initiate infection (Fig. 4A). We observed similar efficiencies in pilus detachment and phage adsorption to the pilus for both WT PP7 and UV-PP7 (Fig. 1, B and F). This further implies that the pilus can be affected by the noninfectious particles where the Mat—probably because of its physical size and shape as well as the orientation of Mat binding to pilin—is the critical factor for pilus detachment.

Our data show that successful pilus detachment requires force provided by retraction

ATPases to pull the T4P-bound phage toward the cell interior. The Mat-pilin interaction must then be strong enough to overcome the strong pilin-pilin interaction for successful infection. Subsequently, phage entry induces pilus bending followed by the pilus detachment event (Fig. 4A).

Discussion

In this work, we observed that a bacterial pilus, T4P, can be removed from the host cell by an ssRNA phage. Our work further suggests that the motility of *P. aeruginosa* is compromised by PP7 phage, noninfectious PP7 particles, or the PP7 maturation protein (Mat) alone.

The retraction ATPases PilT and PilU are required for generating the force required for T4P detachment and phage entry into the host cell. To break the pilus, not only does the force have to reach the critical value, a minimal amount of work also has to be provided by the ATPase to separate the adjacent pilins beyond the breaking point (supplementary text).

We have shown that mature PP7 phages possess two Mat molecules (Fig. 3), with one exposed for T4P binding and another internalized within the capsid, challenging the understanding of the structure of mature ssRNA phages. The assembly of PP7 exhibits considerable plasticity in vRNA conformations, leading to high heterogeneity that currently prevents accurate modeling of the complete vRNA. Previous studies have shown that mature ssRNA coliphages possess more homogeneous, well-defined vRNA (13, 24). The reason for the pronounced heterogeneity of PP7 vRNA in mature virions, compared with other ssRNA phages, is not known. It is yet to be tested whether this heterogeneity plays a role in enhancing the fitness of PP7 during the infection process. A more detailed comparison of ssRNA coliphages and PP7 is provided in the supplementary materials (fig. S11 and supplementary text).

Mat_{IN} interacts with the R1 stem loop preceding the 3' untranslated region of the vRNA. This observation is consistent with the prior finding that an internalized Coat dimer binds to the R1 stem loop in another ssRNA phage, Q β (34). Such an interaction may stabilize the vRNA because the vRNA around this region is conformationally more homogeneous. Alternatively, the Mat dimer interaction may stabilize the conformation of Mat_{EX}, facilitating the proper adsorption and detachment of T4P during entry. These hypotheses are yet to be tested.

In general, the pilus extends and retracts through the narrow channel (typically ranging from ~7 to 15 nm in diameter) of the basal body embedded in the cell envelope (1, 2, 4, 33, 35, 36). In the retraction process, the pilin polymer depolymerizes into the inner membrane at the base of the basal body (1). ssRNA phages (typically ~25 nm in diameter) interfere with the retraction process by the binding of the virion-mounted Mat protein to the side of the pilus. The virion is then passively pulled to the cell surface during pilus retraction. It is evident from the steric constraints depicted in Fig. 4A that the entry of the Mat-pilin complex into the basal body requires pilus detachment. The entry of vRNA presumably ensues because of the binding of Mat to its 3' end (Fig. 2). Because all ssRNA phages characterized to date depend on a retractile pilus for infection, we expect pilus detachment to be a universal feature of such infections (1, 2, 4, 17, 33, 35, 36). We expect that the mechanism unveiled in this study is just one example of a ssRNA phage that compromises the virulence of its bacterial pathogen host while ensuring its own replication.

Materials and methods summary

The full list of materials and detailed methods are provided in the supplementary materials. In brief, the PAOI mutants in this study were constructed as previously described (37). The PP7 bacteriophage was prepared as a large-scale lysate, before concentrated and purified by using CsCl-gradient ultracentrifugation.

To label T4P for fluorescence microscopy imaging, freshly grown PAOI *pilA*-A86C was incubated with a working stock of C5-maleimide Alexafluor-488 (5 mg/ml) and washed twice with LB before imaging. Imaging was performed on a Nikon Eclipse Ti2 inverted epifluorescence microscope by using a 100× objective (Plan Apochromat, NA 1.45, oil immersion) and acquired by use of a cooled electron-multiplying charge-coupled device (EMCCD) camera. All images were taken with the microscope built in 1.5× magnification. Cells were imaged under the phase contrast and with the following fluorescent filter cubes: green filter (485/25×, 525/30m) and mCherry filter (560/40×, 630/75m).

To perform T4P detachment assay, labeled *P. aeruginosa* cells were placed into prewarmed tubes at 37°C before a small aliquot of purified PP7 or equivalent buffer was added to the culture at different MOIs. Infections were performed without shaking to minimize pilus agitation. Samples were removed at indicated time points, and each sample was prepared for microscopy following established protocols. Samples were imaged at multiple stage positions (between 8 and 20 per sample) in phase-contrast and green channels at a series of Z positions. The images were ana-

lyzed with NIS-Elements software (Nikon) for cell and pili counts.

To observe twitching motility without fluorescence, 100 µl of the log-phase cells [optical density of a sample measured at a wavelength of 600 nm (OD_{600}) = 0.4] were dispensed into microcentrifuge tubes and incubated without shaking for 45 min at 37°C to allow a similar condition as that of T4P labeling. Incubated cells were then diluted 1:1.6 with fresh LB before being aliquoted into each empty microcentrifuge tube and treated with either PP7/UV-PP7 at MOI = 5 or 50, or equivalent buffer, and allowed to incubate for 5 or 20 min without shaking in a 37°C water bath. Afterward, the sample was collected and pelleted by means of centrifugation at 6000g for 30 s by means of tabletop centrifuge. The supernatant was discarded, and the pellet was resuspended in ~5 µl of LB. The suspension was spotted onto a 1-mm-thick 0.5% agarose pad dissolved in LB on top of a small coverslip (18 by 18 mm), and overlaid with a large coverslip (24 by 50 mm). The samples were placed into a custom heat chamber (Okolab stage top incubator) set to 30°C and placed under the microscope and imaged under phase contrast every 1 s for 1 min. To observe T4P dynamics, cells were labeled and treated with PP7/UV-PP7 at MOI = 5 or 50, or equivalent buffer as previously described, for 5 or 20 min without shaking. The sample was then pelleted by means of centrifugation at 6000g for 30 s. The supernatant was discarded, and the pellet was resuspended in ~5 µl of LB. Samples were prepared for microscopy as described above. Cells were imaged at 3-s intervals for 1 min at 30°C unless otherwise indicated.

To perform RNA smFISH, a set of probes targeting the full-length PP7 genome was designed. The probes were designed with a 3'mdC [triethylene glycol (TEG)-amino] modification to enable labeling with Alexa Fluor 568 NHS Ester following previously described protocols (38). The labeled probes were then used to detect PP7 RNA during infection. The infected cells were harvested and fixed for imaging according to the established protocol.

Images exported from each experiment were imported into MicrobeJ (39) as hyperstacks for further analyses. Maxima detection function was used to detect phage vRNA signals. Fluorescent foci detection was done on the mCherry channel with a local background filter applied. The thresholds were set according to the negative control. Basically, the threshold would be adjusted to ensure that no cell-associated spots were recognized across buffer-treated samples. The threshold value was then kept throughout the experiments performed on the same date. Afterward, recognized foci for each sample were manually curated to avoid false-positive signals. The number of cells showing cell-associated signals

were then exported and plotted with MATLAB 2022b. For fluorescent signal location analysis and polar signal quantification, local maxima detection was done as above in MicrobeJ with Gaussian fit and edge exclusion. Exported fluorescent spot coordinates information was then allocated to cell segmentation structure obtained from Oufi (40). Cells were segmented and manually refined with precise cell contour recognitions, in which the microbeJ exported spot *xy* coordinates were projected onto the centerline of the corresponding cell, recorded as relative coordinates under the cell structure. Cell centroids have *x* axis values of 0, and the two poles were assigned as 1. Polar signals were defined as spots with *x* values larger than 0.8. Future poles (mid-cells) were defined as spots with *x* values between 0 and 0.1. The fluorescent intensity of individual PP7 vRNA as spots were calculated on the basis of the square of 7 by 7 pixels around the *xy* coordinates obtained from MicrobeJ local maxima detection. Summed fluorescence intensity was then subtracted by the average background intensity, and the same spot was compared across *z* slices to calculate the *z* maxima as the spot intensity.

Optical trap experiments were performed as described previously (32). In brief, overnight cultures were back-diluted 1:50 into fresh LB and grown for 3 hours at room temperature. Before each experiment, cells were mixed with a 1:10,000 dilution of 532-nm polystyrene beads and flushed into a sandwich slide prepared with double-sided sticky tape between a microscope slide and a coverslip. A single bead was optically trapped in the center of a focused laser beam and brought into proximity of the pole of a cell. T4P readily bind polystyrene and upon retraction pulls the trapped bead out of the center of the optical trap against the spring-like optical restoring forces. Pilus retractions were identified through a rapid displacement of the trapped bead toward the pole. We measured this displacement out of the trap center interferometrically and used a standard force-displacement calibration to determine the equivalent retraction stall force of individual T4P (32, 41). The stall force of individual bead displacements (pilus retractions) was analyzed in the software Igor Pro (Wavemetrics).

To perform time-lapse single-cell twitching analysis, image sequences exported from each movie were first analyzed by using the deep-learning model generated with TensorFlow for automatic cell segmentation (42). Exported cell binary masks were then imported into FIJI to use the TrackMate (43) plug-in for cell tracking and cell statistics analysis. Cell tracking was done with a tracking duration threshold of 20 frames to avoid the impact of occasional cell recognition errors. Cell centroid information and individual trajectories were saved as

CSV tables and imported into MATLAB 2022b for statistical analysis and plotting. Single-cell twitching experiments were plotted as a swarm chart with a box plot overlay.

To determine the cryo-EM structure of PP7, the purified PP7 was vitrified and imaged by using Titan Krios with a K3-camera. The images were then processed with RELION. To determine the cryo-EM structures of T4P_{PAOI} and PP7/T4P_{PAOI} complex, the purified T4P_{PAOI} was incubated with PP7 at 37°C for 40 min. The mixture was then vitrified and imaged with stage-tilts at 0°, 15°, and 30°. For PP7/T4P_{PAOI} complex, images collected at all tilt angles were used during processing. For T4P_{PAOI} structure, only images at 0° were used during data processing with RELION and cryoSPARC.

REFERENCES AND NOTES

1. L. L. Burrows, *Pseudomonas aeruginosa* twitching motility: Type IV pili in action. *Annu. Rev. Microbiol.* **66**, 493–520 (2012). doi: [10.1146/annurev-micro-092611-150055](https://doi.org/10.1146/annurev-micro-092611-150055); pmid: [22746331](https://pubmed.ncbi.nlm.nih.gov/22746331/)
2. Y. W. Chang *et al.*, Architecture of the type IVa pilus machine. *Science* **351**, aad2001 (2016). doi: [10.1126/science.aad2001](https://doi.org/10.1126/science.aad2001); pmid: [26965631](https://pubmed.ncbi.nlm.nih.gov/26965631/)
3. M. E. Ryan, P. P. Damke, C. L. Shaffer, DNA transport through the dynamic type IV secretion system. *Infect. Immun.* **91**, e0043622 (2023). doi: [10.1128/iai.00436-22](https://doi.org/10.1128/iai.00436-22); pmid: [37338415](https://pubmed.ncbi.nlm.nih.gov/37338415/)
4. T. Shanmugasundarasamy, D. Karaiyagowder Govindarajan, K. Kandaswamy, A review on pilus assembly mechanisms in Gram-positive and Gram-negative bacteria. *Cell Surf.* **8**, 100077 (2022). doi: [10.1016/j.tcsu.2022.100077](https://doi.org/10.1016/j.tcsu.2022.100077); pmid: [35493982](https://pubmed.ncbi.nlm.nih.gov/35493982/)
5. T. R. D. Costa *et al.*, Structure of the bacterial sex F pilus reveals an assembly of a stoichiometric protein-phospholipid complex. *Cell* **166**, 1436–1444.e10 (2016). doi: [10.1016/j.cell.2016.08.025](https://doi.org/10.1016/j.cell.2016.08.025); pmid: [27610568](https://pubmed.ncbi.nlm.nih.gov/27610568/)
6. M. Clarke, L. Maddera, R. L. Harris, P. M. Silverman, F-pili dynamics by live-cell imaging. *Proc. Natl. Acad. Sci. U.S.A.* **105**, 17978–17981 (2008). doi: [10.1073/pnas.0806786105](https://doi.org/10.1073/pnas.0806786105); pmid: [19004777](https://pubmed.ncbi.nlm.nih.gov/19004777/)
7. K. Goldlust *et al.*, The F pilus serves as a conduit for the DNA during conjugation between physically distant bacteria. *Proc. Natl. Acad. Sci. U.S.A.* **120**, e2310842120 (2023). doi: [10.1073/pnas.2310842120](https://doi.org/10.1073/pnas.2310842120); pmid: [37963249](https://pubmed.ncbi.nlm.nih.gov/37963249/)
8. F. Wang *et al.*, Cryoelectron microscopy reconstructions of the *Pseudomonas aeruginosa* and *Neisseria gonorrhoeae* type IV pili at sub-nanometer resolution. *Structure* **25**, 1423–1435.e4 (2017). doi: [10.1016/j.str.2017.07.016](https://doi.org/10.1016/j.str.2017.07.016); pmid: [28877506](https://pubmed.ncbi.nlm.nih.gov/28877506/)
9. M. D. Koch, C. Fei, N. S. Wingreen, J. W. Shaevitz, Z. Gitai, Competitive binding of independent extension and retraction motors explains the quantitative dynamics of type IV pili. *Proc. Natl. Acad. Sci. U.S.A.* **118**, e2014926118 (2021). doi: [10.1073/pnas.2014926118](https://doi.org/10.1073/pnas.2014926118); pmid: [33593905](https://pubmed.ncbi.nlm.nih.gov/33593905/)
10. International Committee on Taxonomy of Viruses, *Virus Taxonomy: Classification and Nomenclature of Viruses: Ninth Report of the International Committee on Taxonomy of Viruses*, A. M. Q. King *et al.*, Eds. (Academic Press, 2012), pp. 1035–1043.
11. K. R. Chamakura *et al.*, Rapid de novo evolution of lysis genes in single-stranded RNA phages. *Nat. Commun.* **11**, 6009 (2020). doi: [10.1038/s41467-020-19860-0](https://doi.org/10.1038/s41467-020-19860-0); pmid: [33243984](https://pubmed.ncbi.nlm.nih.gov/33243984/)
12. R. I. Koning *et al.*, Asymmetric cryo-EM reconstruction of phage MS2 reveals genome structure in situ. *Nat. Commun.* **7**, 12524 (2016). doi: [10.1038/ncomms12524](https://doi.org/10.1038/ncomms12524); pmid: [27561669](https://pubmed.ncbi.nlm.nih.gov/27561669/)
13. X. Dai *et al.*, In situ structures of the genome and genome-delivery apparatus in a single-stranded RNA virus. *Nature* **541**, 112–116 (2017). doi: [10.1038/nature20589](https://doi.org/10.1038/nature20589); pmid: [27992877](https://pubmed.ncbi.nlm.nih.gov/27992877/)
14. R. Meng *et al.*, Structural basis for the adsorption of a single-stranded RNA bacteriophage. *Nat. Commun.* **10**, 3130 (2019). doi: [10.1038/s41467-019-11126-8](https://doi.org/10.1038/s41467-019-11126-8); pmid: [31311931](https://pubmed.ncbi.nlm.nih.gov/31311931/)
15. K. V. Gorzelnik *et al.*, Asymmetric cryo-EM structure of the canonical Alloviruses Q β reveals a single maturation protein and the genomic ssRNA in situ. *Proc. Natl. Acad. Sci. U.S.A.* **113**, 11519–11524 (2016). doi: [10.1073/pnas.1609482113](https://doi.org/10.1073/pnas.1609482113); pmid: [27671640](https://pubmed.ncbi.nlm.nih.gov/27671640/)
16. J. Y. Chang, K. V. Gorzelnik, J. Thongchol, J. Zhang, Structural assembly of Q β virion and its diverse forms of virus-like particles. *Viruses* **14**, 225 (2022). doi: [10.3390/v14020225](https://doi.org/10.3390/v14020225); pmid: [35215818](https://pubmed.ncbi.nlm.nih.gov/35215818/)
17. L. Harb *et al.*, ssRNA phage penetration triggers detachment of the F-pilus. *Proc. Natl. Acad. Sci. U.S.A.* **117**, 25751–25758 (2020). doi: [10.1073/pnas.2011901117](https://doi.org/10.1073/pnas.2011901117); pmid: [32989140](https://pubmed.ncbi.nlm.nih.gov/32989140/)
18. D. E. Bradley, Shortening of *Pseudomonas aeruginosa* pili after RNA-phage adsorption. *J. Gen. Microbiol.* **72**, 303–319 (1972). doi: [10.1099/00221287-72-2-303](https://doi.org/10.1099/00221287-72-2-303); pmid: [4627885](https://pubmed.ncbi.nlm.nih.gov/4627885/)
19. B. Huang, C. B. Whitchurch, J. S. Mattick, FimX, a multidomain protein connecting environmental signals to twitching motility in *Pseudomonas aeruginosa*. *J. Bacteriol.* **185**, 7068–7076 (2003). doi: [10.1128/JB.185.24.7068-7076.2003](https://doi.org/10.1128/JB.185.24.7068-7076.2003); pmid: [14645265](https://pubmed.ncbi.nlm.nih.gov/14645265/)
20. S. J. Pamp, T. Tolker-Nielsen, Multiple roles of biosurfactants in structural biofilm development by *Pseudomonas aeruginosa*. *J. Bacteriol.* **189**, 2531–2539 (2007). doi: [10.1128/JB.01515-06](https://doi.org/10.1128/JB.01515-06); pmid: [1720224](https://pubmed.ncbi.nlm.nih.gov/1720224/)
21. C. Holz *et al.*, Multiple pilus motors cooperate for persistent bacterial movement in two dimensions. *Phys. Rev. Lett.* **104**, 178104 (2010). doi: [10.1103/PhysRevLett.104.178104](https://doi.org/10.1103/PhysRevLett.104.178104); pmid: [20482147](https://pubmed.ncbi.nlm.nih.gov/20482147/)
22. M. J. Kühn *et al.*, Mechanotaxis directs *Pseudomonas aeruginosa* twitching motility. *Proc. Natl. Acad. Sci. U.S.A.* **118**, e2101759118 (2021). doi: [10.1073/pnas.2101759118](https://doi.org/10.1073/pnas.2101759118); pmid: [34301869](https://pubmed.ncbi.nlm.nih.gov/34301869/)
23. J. Thongchol, Z. Lill, Z. Hoover, J. Zhang, Recent advances in structural studies of single-stranded RNA bacteriophages. *Viruses* **15**, 1985 (2023). doi: [10.3390/v15101985](https://doi.org/10.3390/v15101985); pmid: [37896763](https://pubmed.ncbi.nlm.nih.gov/37896763/)
24. J. Y. Chang *et al.*, Hierarchical natural move Monte Carlo refines flexible RNA structures into cryo-EM densities. *RNA* **26**, 1755–1766 (2020). doi: [10.1261/rna.071100.119](https://doi.org/10.1261/rna.071100.119); pmid: [32826323](https://pubmed.ncbi.nlm.nih.gov/32826323/)
25. K. Tomita, Structures and functions of Q β replicase: Translation factors beyond protein synthesis. *Int. J. Mol. Sci.* **15**, 15552–15570 (2014). doi: [10.3390/ijms150915552](https://doi.org/10.3390/ijms150915552); pmid: [25184952](https://pubmed.ncbi.nlm.nih.gov/25184952/)
26. D. K. Poria, P. S. Ray, RNA-protein UV-crosslinking Assay. *Bio Protoc.* **7**, e2193 (2017). doi: [10.21769/BioProtoc.2193](https://doi.org/10.21769/BioProtoc.2193); pmid: [28580375](https://pubmed.ncbi.nlm.nih.gov/28580375/)
27. M. Götz *et al.*, Single nucleotide resolution RNA-protein cross-linking mass spectrometry: A simple extension of the CLIR-MS workflow. *Anal. Chem.* **93**, 14626–14634 (2021). doi: [10.1021/acs.analchem.1c02384](https://doi.org/10.1021/acs.analchem.1c02384); pmid: [34714631](https://pubmed.ncbi.nlm.nih.gov/34714631/)
28. Ö. Rolfsson *et al.*, Direct evidence for packaging signal-mediated assembly of bacteriophage MS2. *J. Mol. Biol.* **428** (2 Pt B), 431–448 (2016). doi: [10.1016/j.jmb.2015.11.014](https://doi.org/10.1016/j.jmb.2015.11.014); pmid: [26608810](https://pubmed.ncbi.nlm.nih.gov/26608810/)
29. P. Chiang *et al.*, Functional role of conserved residues in the characteristic secretion NTPase motifs of the *Pseudomonas aeruginosa* type IV pilus motor proteins PilB, PilT and PilU. *Microbiology (Reading)* **154**, 114–126 (2008). doi: [10.1099/mic.0.2007/011320-0](https://doi.org/10.1099/mic.0.2007/011320-0); pmid: [18174131](https://pubmed.ncbi.nlm.nih.gov/18174131/)
30. B. Maier, M. Koomey, M. P. Sheetz, A force-dependent switch reverses type IV pilus retraction. *Proc. Natl. Acad. Sci. U.S.A.* **101**, 10961–10966 (2004). doi: [10.1073/pnas.0402305101](https://doi.org/10.1073/pnas.0402305101); pmid: [15256598](https://pubmed.ncbi.nlm.nih.gov/15256598/)
31. B. Maier *et al.*, Single pilus motor forces exceed 100 pN. *Proc. Natl. Acad. Sci. U.S.A.* **99**, 16012–16017 (2002). doi: [10.1073/pnas.242523299](https://doi.org/10.1073/pnas.242523299); pmid: [12446837](https://pubmed.ncbi.nlm.nih.gov/12446837/)
32. M. D. Koch, M. E. Black, E. Han, J. W. Shaevitz, Z. Gitai, *Pseudomonas aeruginosa* distinguishes surfaces by stiffness using retraction of type IV pili. *Proc. Natl. Acad. Sci. U.S.A.* **119**, e2119434119 (2022). doi: [10.1073/pnas.2119434119](https://doi.org/10.1073/pnas.2119434119); pmid: [35561220](https://pubmed.ncbi.nlm.nih.gov/35561220/)
33. M. McCallum, S. Tammam, J. L. Rubinstein, L. L. Burrows, P. L. Howell, CryoEM map of *Pseudomonas aeruginosa* PilQ enables structural characterization of TsaP. *Structure* **29**, 457–466.e4 (2021). doi: [10.1016/j.str.2020.11.019](https://doi.org/10.1016/j.str.2020.11.019); pmid: [33338410](https://pubmed.ncbi.nlm.nih.gov/33338410/)
34. Z. Cui *et al.*, Structures of Q β virions, virus-like particles, and the Q β -MurA complex reveal internal coat proteins and the mechanism of host lysis. *Proc. Natl. Acad. Sci. U.S.A.* **114**, 11697–11702 (2017). doi: [10.1073/pnas.1707102114](https://doi.org/10.1073/pnas.1707102114); pmid: [29078304](https://pubmed.ncbi.nlm.nih.gov/29078304/)
35. K. Macé *et al.*, Cryo-EM structure of a type IV secretion system. *Nature* **607**, 191–196 (2022). doi: [10.1038/s41586-022-04859-y](https://doi.org/10.1038/s41586-022-04859-y); pmid: [35732732](https://pubmed.ncbi.nlm.nih.gov/35732732/)
36. V. A. Gold, R. Salzer, B. Averhoff, W. Kühlbrandt, Structure of a type IV pilus machinery in the open and closed state. *eLife* **4**, e07380 (2015). doi: [10.7554/eLife.07380](https://doi.org/10.7554/eLife.07380); pmid: [25997099](https://pubmed.ncbi.nlm.nih.gov/25997099/)
37. L. R. Hmelo *et al.*, Precision-engineering the *Pseudomonas aeruginosa* genome with two-step allelic exchange. *Nat. Protoc.* **10**, 1820–1841 (2015). doi: [10.1038/nprot.2015.115](https://doi.org/10.1038/nprot.2015.115); pmid: [26492139](https://pubmed.ncbi.nlm.nih.gov/26492139/)
38. S. O. Skinner, L. A. Sepúlveda, H. Xu, I. Golding, Measuring mRNA copy number in individual *Escherichia coli* cells using single-molecule fluorescent in situ hybridization. *Nat. Protoc.* **8**, 1100–1113 (2013). doi: [10.1038/nprot.2013.066](https://doi.org/10.1038/nprot.2013.066); pmid: [23680982](https://pubmed.ncbi.nlm.nih.gov/23680982/)
39. A. Ducret, E. M. Quardokus, Y. V. Brun, MicrobeJ, a tool for high throughput bacterial cell detection and quantitative analysis. *Nat. Microbiol.* **1**, 16077 (2016). doi: [10.1038/nmicrobiol.2016.77](https://doi.org/10.1038/nmicrobiol.2016.77); pmid: [27572972](https://pubmed.ncbi.nlm.nih.gov/27572972/)
40. A. Paintdakhi *et al.*, Outfit: An integrated software package for high-accuracy, high-throughput quantitative microscopy analysis. *Mol. Microbiol.* **99**, 767–777 (2016). doi: [10.1111/mmi.13264](https://doi.org/10.1111/mmi.13264); pmid: [26538279](https://pubmed.ncbi.nlm.nih.gov/26538279/)
41. M. D. Koch, J. W. Shaevitz, Introduction to optical tweezers. *Methods Mol. Biol.* **1486**, 3–24 (2017). doi: [10.1007/978-1-4939-6421-5_1](https://doi.org/10.1007/978-1-4939-6421-5_1); pmid: [27844423](https://pubmed.ncbi.nlm.nih.gov/27844423/)
42. K. Zhang *et al.*, Interactions between viral regulatory proteins ensure an MOI-independent probability of lysogeny during infection by bacteriophage ϕ 1. *mBio* **12**, e0101321 (2021). doi: [10.1128/mBio.01013-21](https://doi.org/10.1128/mBio.01013-21); pmid: [34517752](https://pubmed.ncbi.nlm.nih.gov/34517752/)
43. D. Ershov *et al.*, TrackMate 7: Integrating state-of-the-art segmentation algorithms into tracking pipelines. *Nat. Methods* **19**, 829–832 (2022). doi: [10.1038/s41592-022-01507-1](https://doi.org/10.1038/s41592-022-01507-1); pmid: [35654950](https://pubmed.ncbi.nlm.nih.gov/35654950/)
44. J. Thongchol, Z. Yu, Y. Wu, J. Zhang, L. Zeng, Data supporting the paper 'Removal of *Pseudomonas* type IV pili by a Small RNA virus'. Zenodo (2024); <https://doi.org/10.5281/zenodo.10638490>
45. J. Thongchol, jirapatt/Codes-and-Scripts: Codes and Scripts Supporting The Paper 'Removal of *Pseudomonas* Type IV Pili by a Small RNA Virus'. Zenodo. (2024); <https://doi.org/10.5281/zenodo.10845966>

ACKNOWLEDGMENTS

We thank J. Zhu and X. Zhang for helping to perform the RNA gel experiment and R. Barnshaw and L. L. Burrows for discussions. We express our sincere appreciation to E. S. Kim and Y.-H. Cho for their contribution of *Pseudomonas aeruginosa* Δ pilA strains. We thank Z. Cui, M. Jiang, J.-Y. Chang, and R. Meng for their help in the early screening of the cryo-EM sample. Additionally, we extend our thanks to P. Mitchell and S. Li from Stanford-SLAC Cryo-EM Center (S2C2) and G. Yadav from the Texas A&M University Laboratory for Biomolecular Structure and Dynamics (LBSD) for their assistance in cryo-EM data collection. The LBSD is supported in part by the Department of Biochemistry and Biophysics, AgriLife, and Texas A&M University. We also acknowledge the MIC at ILSB, Texas A&M University, for their support in conducting the initial cryo-EM screening. Furthermore, we are grateful to the Texas A&M High Performance Research Computing Center for providing the computational resources required for data processing. We thank all members of the Zhang and Zeng laboratories for discussions. We also thank undergraduate students—including M. Kretiv, M. Frye, A. Mills, and C. Hanson—who helped us replicate experiments. We thank R. Young, P. Christie, L. L. Burrows, and X. Zhang for commenting on the earlier version of this manuscript. **Funding:** This work was supported by National Institutes of Health grant R01GM141659 (Y.W., J.Z., and L.Z.); National Institutes of Health grant R21AI156846 (J.Z. and L.Z.); National Science Foundation grant MCB-1902392 (J.Z. and L.Z.); Texas A&M University T3 grant (J.Z. and L.Z.); a Texas A&M University X-grant (J.Z. and L.Z.); the Center for Phage Technology, jointly sponsored by Texas AgriLife and Texas A&M University (J.Z. and L.Z.); Welch Foundation grant A1863 (J.Z.); and the National Science Foundation, through the Center for the Physics of Biological Function, PHY-1734030 (J.S.). **Author contributions:** Conceptualization: J.T., Z.Y., L.H., Y.L., M.T., J.Z., and L.Z. Investigation: J.T., Z.Y., L.H., M.K., U.N., Y.W., J.Z., and L.Z. Funding acquisition: J.S., Y.W., J.Z., and L.Z. Supervision: J.Z. and L.Z. Writing – original draft: J.T., Z.Y., L.H., M.K., Y.L., Y.W., J.Z., and L.Z. Writing – review and editing: J.T., Z.Y., L.H., Y.L., M.T., M.K., J.S., Z.G., Y.W., J.Z., and L.Z. **Competing interests:** J.Z. is a consultant of Lynntech, College Station, Texas. Z.G. is the scientific founder, board member, consultant, and scientific advisory board chair of ArrePath, Princeton, New Jersey. **Data and materials availability:** The structural

models of PP7, T4P_{PAO1}, and the Mat/T4P_{PAO1} complex have been deposited in the Protein Data Bank (PDB) with PDB codes 8TUX, 8TUM, and 8TUW, respectively. The structural model for Mat/PilA^{PAO1} complex from RosettaDock is available at Zenodo (44). The cryo-EM density maps have been submitted to the Electron Microscopy Data Bank (EMD) with accession codes EMD-41632 (PP7), EMD-41625 (T4P_{PAO1}), EMD-41675 (original map of PP7/T4P_{PAO1} complex), EMD-41633 (local refined map of PP7/T4P_{PAO1} complex), and EMD-41780 (composite map of PP7/T4P_{PAO1} complex). The additional cryo-EM data collection parameters, refinement, and validation statistics are summarized as shown in table S3. Fluorescence microscopy

data are also available at Zenodo (44). This work also used Custom MATLAB scripts to calculate the intensity and relative position of the fluorescent foci and a python script by using a pretrained weight model to generate cell binary masks for tracking and cell counting. Additionally, we developed an in-house program in FORTRAN for coarse-grained Langevin dynamics simulation to capture the entry state of PP7. All codes and scripts can be found at (45). **License information:** Copyright © 2024 the authors, some rights reserved; exclusive licensee American Association for the Advancement of Science. No claim to original US government works. <https://www.science.org/about/science-licenses-journal-article-reuse>

SUPPLEMENTARY MATERIALS

[science.org/doi/10.1126/science.adl0635](https://doi.org/10.1126/science.adl0635)

Materials and Methods

Supplementary Text

Figs. S1 to S14

Tables S1 to S3

References (46–71)

Movies S1 to S6

MDAR Reproducibility Checklist

Submitted 29 September 2023; accepted 29 February 2024
10.1126/science.adl0635